Electronic band structure and conduction mechanism of mixed valence Te^{4+}/Te^{6+} pyrochlore oxides

Anurak Waehayee,[1] Narong Chanlek,[2,3,4] Pinit Kidkhunthod,[2,3,4] Hideki Nakajima,[2]
Suwit Suthirakun,[1,3,4] and Theeranun Siritanon[1,3,4,*]

[1]*School of Chemistry, Institute of Science, Suranaree University of Technology, 111 University Avenue, Nakhon Ratchasima, 30000, Thailand*
[2]*Synchrotron Light Research Institute, Nakhon Ratchasima, 30000, Thailand*
[3]*Center of Excellence-Advanced Functional Materials, Suranaree University of Technology, Nakhon Ratchasima, 30000, Thailand*
[4]*Research Network NANOTEC-SUT, Center for Advanced Nanomaterials and Characterization, Suranaree University of technology, Nakhon Ratchasima, 30000, Thailand*

(Received 3 February 2019; revised manuscript received 20 May 2019; published 23 July 2019)

While many post-transition metals could form mixed valence oxides with high conductivities leading to various interesting applications, oxides of tellurium are usually insulators. The only known mixed valence tellurium oxides that show appreciable electronic conductivities are the $Cs(M, Te)_2O_6$ series. However, experimental and theoretical investigations of the compounds are scarce. To study the effects of M metal substitution of tellurium on the structural and electronic properties of $Cs(M, Te)_2O_6$ mixed valence compounds, a series of oxides with the general formula $CsMn_xTe_{2-x}O_6$ have been prepared and characterized. Substituting Te in $CsTe_2O_6$ with as small as 2.5% Mn ($x = 0.05$) changes the structure from rhombohedral to cubic symmetry. Based on the x-ray photoelectron spectroscopy and x-ray absorption near edge structure studies, we found that Mn in the samples with $x \leqslant 0.33$ is in +3 states, while samples with $x > 0.33$ contain a mixture of Mn^{3+} and Mn^{4+}. Detailed studies indicate that there are two substitution schemes depending on the x values. The switching between these two schemes occurs at around $x = 0.30-0.33$, which results in a change in the trend of electronic conductivity. To describe the electronic properties, simple schematic band structure diagrams of the samples are proposed based on experimental results and density functional theory calculations. $CsMn_xTe_{2-x}O_6 (x < 0.33)$ contains Te^{4+}/Te^{6+} mixed valency where both species are in the same crystallographic sites. Yet, the Te 5s band is split into two parts with Te^{4+} contributing to the valence band maximum and Te^{6+} contributing to the conduction band minimum. Such a splitting indicates that they are distinguishable because of a local distortion in the lattice. We found that energy levels of Te^{4+} 5s states relative to the conduction band exhibit a strong correlation with the unit cell parameters. When the cell parameter is small, Te^{4+} is destabilized in the lattice causing its energy level to increase. While metallic conduction has not been achieved in this series of compounds, the detailed investigation in this work deepens the understanding about their electronic structures and sheds light on the possibility of designing type III mixed valence tellurium oxides.

DOI: 10.1103/PhysRevB.100.045132

I. INTRODUCTION

Many modern electronic devices and applications demand materials with good electrical properties and durability. High stability and electronic conduction obtained from the n-type doping in post-transition metal oxides such as In_2O_3, SnO_2, and $ZnSnO_3$ [1–3] allow them to be widely used.These materials can be classified as a type III mixed valence compounds according to Robin and Day classification [4] where the two valences are indistinguishable resulting in a metallic conduction. While similar materials are known for many of the post-transition elements, examples are scarce for tellurium. In fact, most of tellurium mixed valence compounds are type I as Te^{4+} and Te^{6+} are differently coordinated, which leads to them being insulators. To our knowledge, the only type II Te mixed valence oxide is $CsTe_2O_6$, which contains both Te^{4+} and Te^{6+} in similar, but distinguishable, octahedral sites.

Transition from a type II to a type III mixed valency is observed in $BaBiO_3$ system. The compound contained Bi^{3+} and Bi^{5+} with different Bi-O bond distances causing a distortion of the structure [5]. Such a distortion decreases when $BaBiO_3$ is doped with K in $Ba_{1-x}K_xBiO_3$ system. The semiconductor to metal transition occurs at around $x = 0.35$. In the metallic region, the extended x-ray absorption fine structure studies indicate that the Bi^{3+}/Bi^{5+} ordering disappears and only one Bi-O distance is observed [6]. Rhombohedral $CsTe_2O_6$ can be considered an analogy of $BaBiO_3$ as it similarly contains Te^{4+} and Te^{6+} in the lattice [7]. In addition, the usual lone pair distortion is absent for both Bi^{3+} in $BaBiO_3$ and Te^{4+} in $CsTe_2O_6$ [8]. Therefore, a rhombohedral $CsTe_2O_6$ is a very good starting point for investigation of possible type III mixed valence tellurium oxides.

It was recently shown that substitution of Te in $CsTe_2O_6$ with $M(M =$ various metal cations in $+3$ and $+4$ states) in the $Cs(M, Te)_2O_6$ series gives rise to mixed valence tellurium oxides with semiconducting behaviors [9]. Here, the ordering at M/Te site is destroyed giving rise to a cubic unit cell with

*theeranun@sut.ac.th

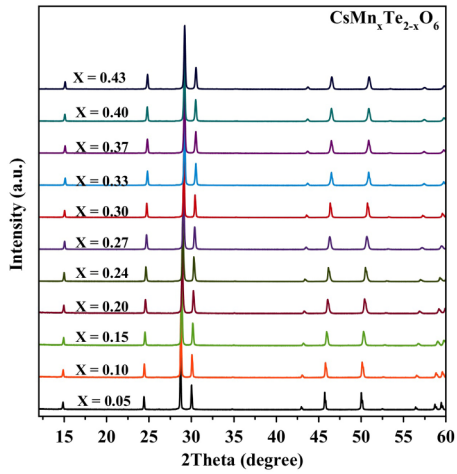

FIG. 1. Powder x-ray diffraction patterns of $CsMn_xTe_{2-x}O_6$.

only one *M*/Te-O bond distance. Although the formula implies that all Te is in +6 state, a slight deviation from stoichiometry generates a small amount of Te^{4+} in the lattice, which creates donor states close to the conduction band leading to an *n*-type character. It is generalized that the smaller unit cell, e.g., the shorter Te-O bond, destabilizes the Te^{4+} donor level moving it closer to the conduction band edge and results in higher conductivity. Among all compounds in the series, only $Cs(Al, Te)_2O_6$ has been extensively studied [10]. While the small Al^{3+} causes donor states in $CsAl_{0.33}Te_{1.67}O_6$ to have high energy level, the number of such states are very low. Nevertheless, $CsAl_{0.33}Te_{1.67}O_6$ exhibits degenerate semiconducting behavior with a conductivity of about 10 Ω cm in a sintered pellet [9]. To the best of our knowledge, the only $Cs(M, Te)_2O_6$ related compounds that form cubic structure with a high content of Te^{4+} is $Cs(W, Te)_2O_6$. However, W^{6+} is found to replace Te^{6+}, which results in larger unit cell parameters and the compounds are not conducting [11].

It is the purpose of this work to investigate the electronic structure of $Cs(Mn, Te)_2O_6$ employing x-ray absorption spectroscopy (XAS), x-ray photoelectron spectroscopy (XPS), and first-principles computation [12–14]. Mn is chosen because our preliminary results indicated that the cubic pyrochlore structure can be achieved with various Mn content. In fact, only 2.5% Mn substitution is enough to trigger a phase transformation from rhombohedral to cubic. Therefore, $Cs(Mn, Te)_2O_6$ would be the second series of compounds with a cubic structure and high Te^{4+} content. In addition, Mn is known to have a variable oxidation state in oxides. Yet, a previous report indicates that $CsMn_{0.33}Te_{1.67}O_6$ shows a much lower conductivity compared to $CsAl_{0.33}Te_{1.67}O_6$. Understanding the valence situation and electronic structure of $Cs(Mn, Te)_2O_6$ would supply knowledge about the conduction mechanism of the rare *n*-doped tellurium oxides, which could lead to the future design of other tellurium containing functional materials.

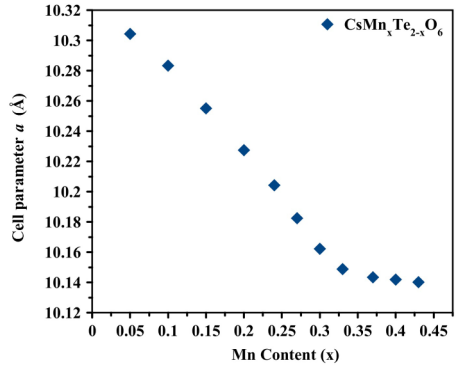

FIG. 2. Changes of cell parameters with the Mn content.

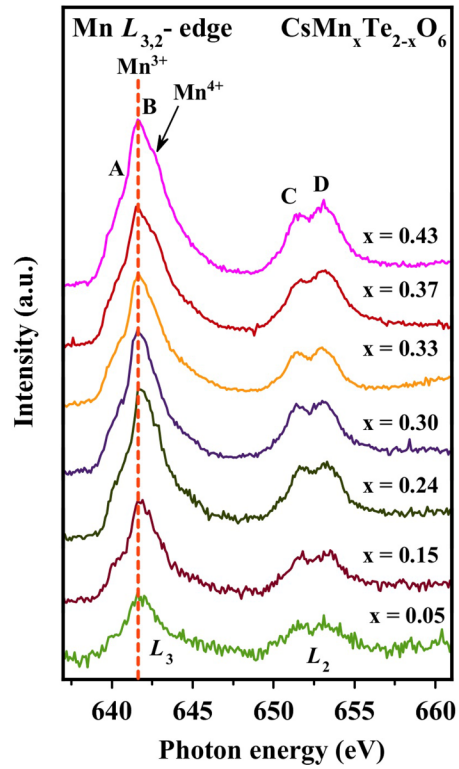

FIG. 3. Mn $L_{3,2}$-edge XANES spectra of $CsMn_xTe_{2-x}O_6$.

II. EXPERIMENT

The solid state reaction method was used to prepare $CsMn_xTe_{2-x}O_6$ series. Stoichiometric amounts of $CsNO_3$ (Sigma-Aldrich, 99+%), Mn_2O_3 (Sigma-Aldrich, 99%), and TeO_2 (Acros organic, 99+%) were ground in an agate mortar and heated at 550 °C for 5 h. After that, the samples were reground and sintered at 625 °C for 24 h in air. Powder x-ray diffraction (XRD) patterns were recorded by a Bruker D2 Phaser diffractometer (Cu Kα radiation, $\lambda = 1.5406$ Å) for phase identification. X-ray absorption near edge structure (XANES) and XPS experiments were carried out at Synchrotron Light Research Institute, Thailand. The Te L_3-edge spectrum was obtained at the BL5.2: SUT-NANOTEC-SLRI XAS Beamline using transmission modes. The Mn $L_{3,2}$-edge and O *K*-edge spectra were obtained at the BL3.2Ua: PES (Photoelectron Emission Spectroscopy) using total electron yield modes. The XPS of Mn 2*p*, Te 3*d*, and valence band (VB) were recorded by a PHI5000 VersaProbe II XPS instrument (ULVAC-PHI, Japan) (Monochromatic x-ray of Al Kα,

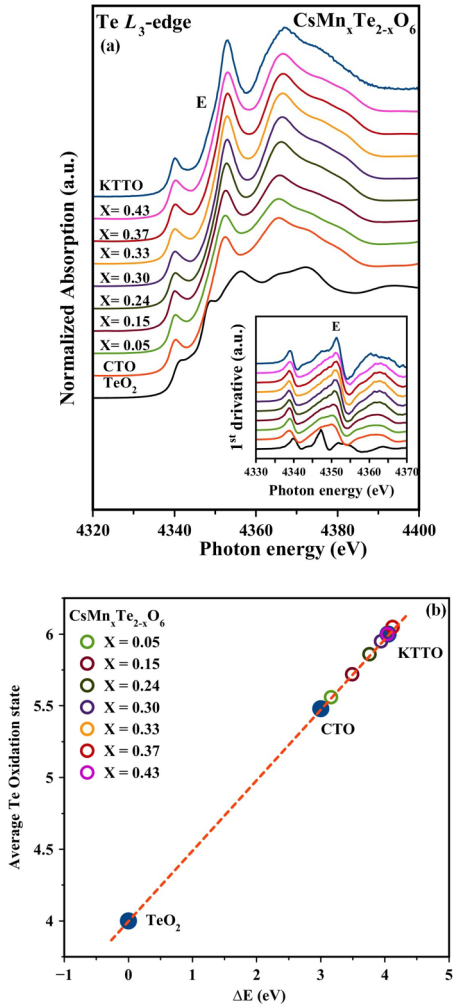

FIG. 4. (a) Te L_3-edge XANES and first derivative spectra (inset) of $CsMn_xTe_{2-x}O_6$. (b) A calibration curve used to estimate average oxidation state of Te in the samples.

1486.6 eV) at BL5.3: SUT-NANOTEC-SLRI. The C 1*s* at 284.8 eV was used as a reference for the binding energies drift due to charging effects. The electrical conductivities of all sintered samples were measured from 298 to 673 K by a four-probe method using a Keysight B2901A source/measure unit.

III. COMPUTATIONAL DETAILS

To further explore the electronic structure of the $CsMn_xTe_{2-x}O_6$ cubic pyochlores, we calculated the projected density of states (PDOS) of the $CsMn_{0.25}Te_{1.75}O_6$ system. The model was taken from the Rietveld-refined experimental unit cell of $CsTe_2O_6$ containing eight Cs cations, 16 Te cations, and 48 O anions, which corresponds to eight $CsTe_2O_6$ formula unit ($Cs_8Te_{16}O_{48}$) [15]. Then, the $CsMn_{0.25}Te_{1.75}O_6$ model system was achieved by replacing two Te ions with two Mn ions. The foreign Mn ions are expected to statistically distribute at the Te sites, which yield nonequivalent lattice configurations with different total energies. For simplicity, we considered only the configuration depicted in Ref. [16] to represent the $CsMn_{0.25}Te_{1.75}O_6$ structure. While the other lower energy configurations may exist, it is expected that the overall electronic structures are not affected by the positions of the two Mn ions.

The calculated electronic structures reported herein were carried out using spin-polarized density functional theory (DFT+U) with periodic model as implemented in Vienna Ab Initio Simulation Package (VASP 5.3) [17–19]. We employed Dudarev's approach [17] for DFT+U calculations to correct for the self-interaction error inherent in current exchange-correlation functionals DFT when applied to transition metals with tightly localized *d* electrons, such as Mn in the $CsMn_{0.25}Te_{1.75}O_6$ model system. It is known that the proper value of the U parameter varies from system to system and also depends on the interested properties of the system. There have been several studies reporting the use of the U value in the range of 4.0–5.5 eV for studying various properties of bulk and surfaces of MnO_2 [20–23]. In this work, we chose the U value of 4.0 eV for Mn 3*d* electrons as it was used to properly describe the electronic structures of stoichiometric and reduced MnO_2 systems [22]. Exchange correlation is described within the generalized gradient approximation with the Perdue-Burke-Ernzerhof functional [24]. We chose the ultrasoft pseudopotential with the projector augmented wave method to represent the inner core potentials and treated the Cs 5*s*5*p*6*s*, Te 5*s*5*p*, Mn 3*s*3*p*3*d*4*s*, and O 2*s*2*p* as valence electrons [25,26]. Their wave functions were expanded in the plane-wave basis with a cutoff energy of 400 eV. The tetrahedron smearing method with Bloch corrections with a γ-centered k point of $3 \times 3 \times 3$ were used to produce the

TABLE I. Estimated Te^{4+} and Te^{6+} content in $CsMn_xTe_{2-x}O_6$ samples

Mn content	ΔE (eV)	Valence	Te content		Ideal Te content[a]	
			Te^{6+}	Te^{4+}	Te^{6+}	Te^{4+}
0.00 (CTO)	3.00	5.48	1.48	0.52	1.50	0.50
0.05	3.16	5.56	1.52	0.43	1.52	0.43
0.15	3.49	5.72	1.59	0.26	1.57	0.28
0.24	3.76	5.86	1.63	0.13	1.62	0.14
0.30	3.94	5.95	1.65	0.05	1.65	0.05
0.33	4.12	6.05	1.70	−0.03	1.67	0.00
0.37	4.12	6.05	1.66	−0.03	1.63	0.00
0.43	4.04	6.00	1.57	0.00	1.57	0.00

[a]Calculated from $Cs^{1+}(Mn^{3+})_x(Te^{4+})_{0.5-(3x/2)}(Te^{6+})_{1.5+(x/2)}O_6$ for $x = 0.05-0.33$ and from $Cs^{1+}(Mn^{3+/4+})_x(Te^{6+})_{2-x}O_{6-\delta}$ for $x > 0.33$.

PDOS. Using a denser $5 \times 5 \times 5k$ mesh yields a negligible difference in the PDOS results.

IV. RESULTS AND DISCUSSION

Powder x-ray diffraction patterns of all prepared $CsMn_xTe_{2-x}O_6$ samples (Fig. 1) indicate that the single cubic pyrochlore phase is achieved when $x = 0.05-0.43$. The structure can be described as the interpenetrating network of $(Mn/Te)O_6$ octahedra and Cs cation [27]. It is quite unexpected that only 2.5% of Mn is enough to disrupt the ordering of Te^{4+} and Te^{6+} in a rhombohedral $CsTe_2O_6$. As mentioned earlier, substituting Te with W could also alter the symmetry of the structure but at least 10% W content was required [11]. The shift of the diffraction peaks suggest that Mn is incorporated into the lattice. No diffractions due to superstructure or any types of ordering are observed. However, the peak broadening is clearly observed, especially in samples with higher Mn content. Both crystallite size and strain are well known causes of peak broadening. Nevertheless, all samples were prepared by solid state reaction thus their crystallite sizes should be similar and too large to cause peak broadening. On the other hand, the compounds contain various cations with different ionic radii in the same crystallographic site which results in local distortion and lattice strain. In fact, Li *et al.* [10] systematically investigated peak broadening in the $CsAl_xTe_{2-x}O_6$ pyrochlore system and concluded that the observed peak broadening is entirely due to the lattice strain. We carefully calculated the lattice parameters by Le Bail refinement with the use of NaCl internal standard. As depicted in Fig. 2, the relationship between cell parameters and the Mn content form two linear lines with different slopes. This observation suggests that there are two different mechanisms of the Mn substitution with the switching point around $x = 0.33-0.37$.

To further investigate the substitution mechanisms, the oxidation states of Mn in the samples were investigated by XANES. Fig. 3(a) shows the Mn $L_{3,2}$-edge XANES spectra of the samples. The spectra correspond to Mn $2p \rightarrow 3d$ allowed transition and are split into $MnL_3(2p_{3/2})$ and $MnL_2(2p_{1/2})$ because of the spin-obit coupling [28,29]. Each peak is further split into t_{2g} [denoted A and C in Fig. 3(a)] and e_g state [denoted B and D in Fig. 3(a)] due to a crystal field effect. Such a complex spectra feature gives valuable information on Mn in the samples. First of all, the energy positions of the Mn L_3-edge peak of all samples align well with that of Mn^{3+}, indicating that Mn^{3+} is a major component [30]. Furthermore, the intensities of the split peaks reflect the total unoccupied Mn $3d$ state, which can additionally imply the valence situation of Mn [31–33]. The ratio of unoccupied e_g states to unoccupied t_{2g} states is higher in Mn^{4+} than in Mn^{3+} [28,32]. Thus, the increase of the ratios of B/A and D/C indicate the increase of Mn^{4+} content. Here, we observe such increases in both ratios and a different Mn L_3-edge peak corresponding to Mn^{4+} appears in samples with $x > 0.33$, suggesting that these samples contain Mn^{3+}/Mn^{4+} mixed valency. The same conclusion is reached when the samples were characterized with the XPS technique for confirmation [34]. It is interesting to note that this mixed valency appears at the same switching point observed in XRD patterns (Fig. 2).

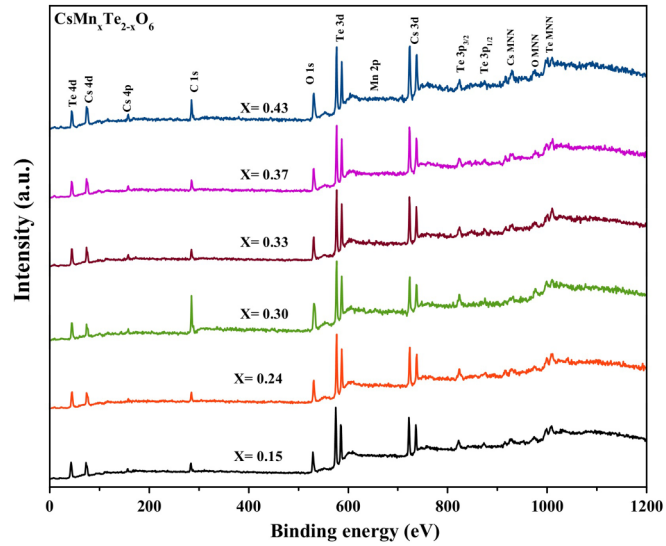

FIG. 5. XPS survey spectra of $CsMn_xTe_{2-x}O_6$.

The Te L_3 -edge XANES spectra were collected to study Te oxidation states [Fig. 4(a)]. With the use of a calibration curve constructed from edge energies of TeO_2 (Te^{4+}), $CsTe_2O_6$ (mixed Te^{4+}/Te^{6+}) and $KTaTeO_6$ (Te^{6+}) [Fig. 4(b)], the Te^{4+}/Te^{6+} ratios in the samples were estimated as summarized in Table I [35]. The analysis of the Te $3d$ XPS spectra also gives similar Te^{4+}/Te^{6+} ratios [36]. Based on both Mn and Te oxidation state investigations, it is obvious that for samples with $x = 0.05-0.33$, Mn^{3+} is replacing Te^{4+} as Te^{4+} content decreases, while that of Te^{6+} increases. One could represent the substitution situation for these samples with the general formula $Cs^{1+}(Mn^{3+})_x(Te^{4+})_{0.5-(3x/2)}(Te^{6+})_{1.5+(x/2)}O_6$. The significant reduction in unit cell parameters of the samples with this range of x are in agreement with this formula considering that the ionic radius of Mn^{3+} (0.645 Å) is much smaller than that of Te^{4+} (0.97 Å), but larger than that of Te^{6+}(0.56 Å) [37,38].

Based on the proposed formula, the maximum value of x is limited at 0.33, after which the substitution mechanism changes. The results summarized in Table I suggest that Mn starts to replace Te^{6+} at this point and we see from Mn $L_{3,2}$-edge XANES that Mn^{4+} is present in the samples. Without additional charge compensation, the presence of Mn^{4+} could balance the charge within the limited x range. For example, at $x = 0.4$, neutrality of the compound is preserved if 50% of Mn is Mn^{4+}. However, this scenario would require a significant amount of Mn^{4+} but we do not see Mn^{4+} as a majority even in a sample with $x = 0.43$. Thus, additional charge compensation must be present. Although several types of defect could occur such as Cs vacancies, Cs interstitials, oxygen vacancies, and oxygen interstitials, only the Cs interstitial and oxygen vacancies result in a lower Mn^{4+} content. Our XRD and transmission electron microscopy (TEM) results [39] indicate no impurity phases of any kind. Thus, the most probable mechanism here is the formation of oxygen vacancies. This would also lead to a less significant change in the cell parameters as observed in Fig. 2. Therefore, the compounds with $x = 0.37-0.43$ may be represented with the

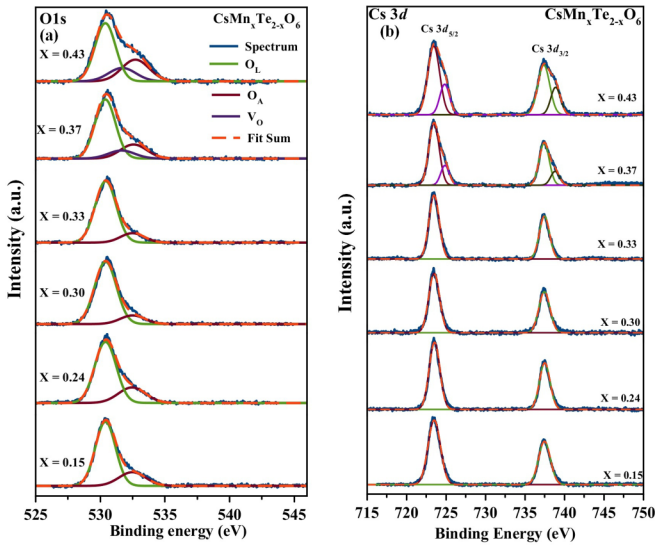

FIG. 6. (a) O 1*s* and (b) Cs 3*d* XPS spectra of $CsMn_xTe_{2-x}O_6$.

general formula $Cs^{1+}(Mn^{3+/4+})_x(Te^{6+})_{2-x}O_{6-\delta}$. The value of δ in this formula is rather small as even without a contribution from Mn^{4+}, only an oxygen vacancy δ of 0.145 is required in a sample with $x = 0.43$. Such an amount of oxygen vacancy is within a limit reported in the defect cubic pyrochlore oxides including $CsTe_2O_6$ [15,40]. Note that the Te^{4+}/Te^{6+} contents calculated from this proposed formula agree well with the numbers estimated from the calibration curve (Table I).

We additionally use XPS to study the samples [Fig. 5]. O 1*s* and Cs 3*d* XPS spectra are shown in Fig. 6. O 1*s* spectra could be deconvoluted into three parts; O_L, V_O, and O_A which correspond to lattice oxygen, oxygen vacancies or hydroxyl, and absorbed oxygen, respectively [41–43]. Cs 3*d* XPS spectra show slightly a different feature for the samples with $x > 0.33$. Similarly, we deconvoluted the spectra to two main components [Fig. 6(a)]. The major component at binding energy ~ 723.5 eV ($Cs3d_{5/2}$) is characteristic of Cs^+ [44]. The small shoulder of Cs $3d_{5/2}$ is at slightly higher binding energy ($\sim$724.8 eV) but still within a range of Cs^+(723.5−725.1 eV) [44,45]. Thus this shoulder may suggest a presence of Cs^+ in different environments, such as Cs^+ in the vicinity of the oxygen vacancies or hydroxyl [46].

Electronic conductivities of the samples were measured from 298 to 673 K and plotted according to the Arrhenius equation [Fig. 7(a)]. The obtained activation energy of conduction is also plotted with a Mn content as shown in Fig. 7(b). The most conducting sample in the series is $CsMn_{0.3}Te_{1.7}O_6$. The conductivities and activation energies generally depend on the cell parameters. The smaller the unit cell parameters, the higher the conductivities. The same trend was also observed in Ref. [9]. However, the conductivity of $CsMn_{0.3}Te_{1.7}O_6$ is lower than that of previously reported $CsGa_{0.33}Te_{1.67}O_6$ despite having similar cell parameters [9] because Mn does not have a diffused *s* orbital like Ga. It is interesting to note that the Mn series in this work generally have smaller cell parameters than the W series [11]. As a result, our samples exhibit higher conductivities. Although oxygen vacancies can often improve electronic conductivity of oxides, it is not the case for this group of tellurium oxide pyrochlores. The $CsTe_2O_{6-x}$ series were not conducting [15] and our samples with $x > 0.33$ do not show any improvement in the conductivities.

To obtain insight into the electronic structures of $CsMn_xTe_{2-x}O_6$ cubic pyrochlores, we computed and analyzed the PDOS of the $CsMn_{0.25}Te_{1.75}O_6$ model system by means of DFT+U calculations and characterized the samples with XPS at the VB region and O *K*-edge XANES. As shown in Fig. 8, the calculated PDOS of the $CsMn_{0.25}Te_{1.75}O_6$ system matches very well with the results obtained from XPS and XANES. At the bottom of the valence band, [denoted A in Figs. 8(a) and 8(c)] the Cs 5*p* states dominate with small contributions from Te 5*p* and O 2*p* states, which is similar to the previous report for $CsTe_2O_6$ [44]. Hybridization between O 2*p*, Mn 3*d*, and Te 5*p* results in the peak denoted B. The positions of this peak slightly shift toward higher energy when the Mn content is increased [Fig. 8(c)]. Two factors that might affect B position are the degree of overlapping and the energy level of Mn 3*d*, both of which are correlated with the unit cell parameters and the environments around Mn/Te including Mn/Te-O distances and Mn/Te-O-Mn/Te angles. The VB top develops its overall character from Mn 3*d* states and Te 5*s* states originated from

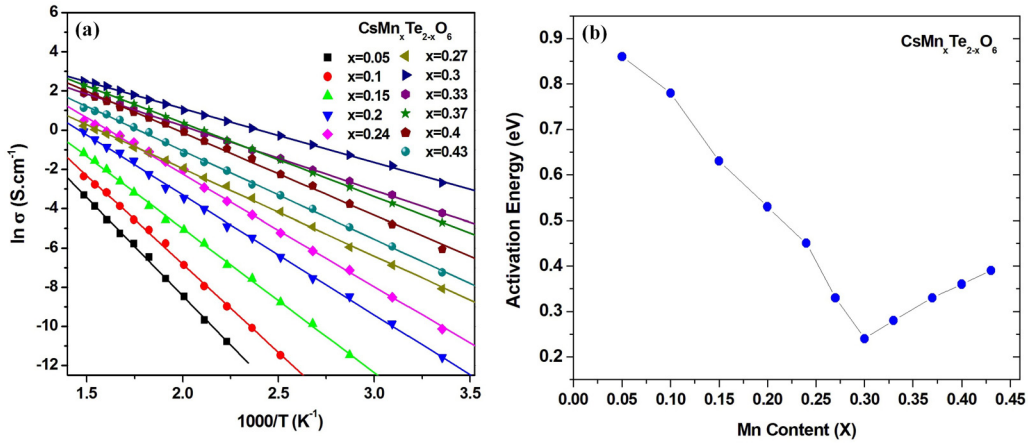

FIG. 7. (a) Arrhenius plots of electronic conductivities and (b) the obtained activation energy of conduction.

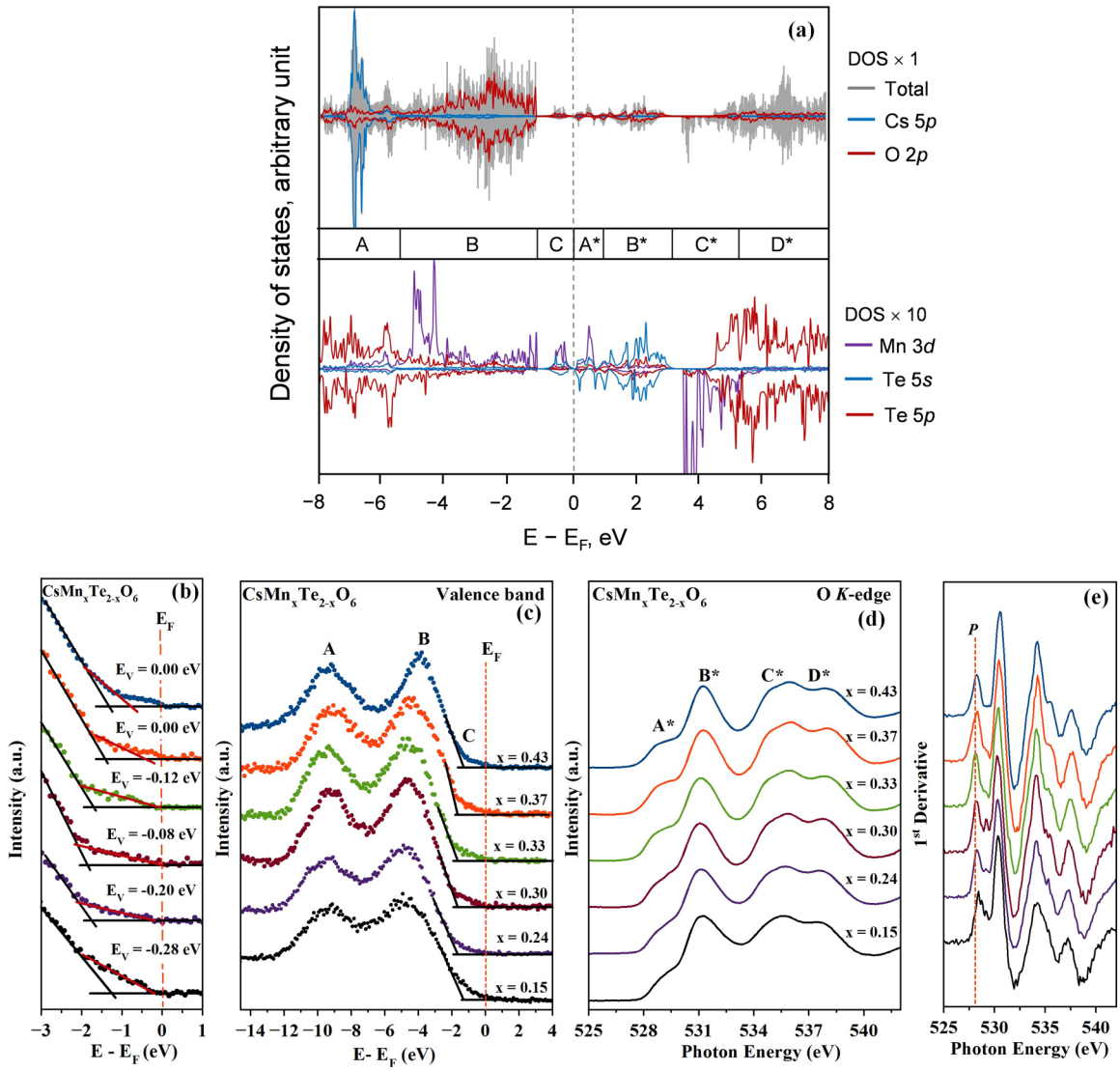

FIG. 8. Calculated PDOS of the $CsMn_{0.25}Te_{1.75}O_6$ system. The energy of the PDOS are plotted with relative to the Fermi energy (a), XPS close-up near E_F (b), Valence band XPS (c), O *K*-edge spectra (d), and the first derivatives of the spectra (e) of $CsMn_xTe_{2-x}O_6$.

Te^{4+} in the sample [C in Figs. 8(a) and 8(c)]. A close-up at the VB maximum (VBM) reveals an additional tailing in the samples with $x > 0.33$, which might be caused by the presence of oxygen vacancies [47]. Changes in the intensity of peak C are related to the change in Te^{4+} and Mn content in each sample.

O *K*-edge XANES spectra is the absorption edge of 1*s* to 2*p* transition in oxygen atom and related to the conduction band of oxides [48,49]. Here, we compare the O *K*-edge XANES spectra with the calculated PDOS. A unique character of the low-lying conduction band is identified where it mainly comprises Te 5*s* states with some contribution from Mn states in the region A* [Figs. 8(a) and 8(d)]. This feature becomes more intense with Mn content, confirming the significance of the Mn 3*d*-O 2*p* hybridization [49–51]. In addition, the first derivative plot [Fig. 8(e)] shows a shift of conduction band minimum when a Mn content changes. The calculated PDOS suggests that the peak denoted B* primarily consists of O 2*p* and Te 5*s*. The split-off conduction band is separated from a broad higher conduction band contributed by Mn 3*d* and Te 5*p* states [denoted C in Figs. 8(a) and 8(d)]. The strong contribution from Mn 3*d* is reflected by the slight increase in the peak intensity in this region when the Mn content increases as shown in the O *K*-edge spectra [Fig. 8(d)]. The region denoted D* is primarily contributed from hybridization of Te 5*p* and O 2*p* states. In addition, DFT calculations reveal the magnetization of 8 μB which indicates that there are in total eight unpaired electrons in the system implying a formation of two Mn^{3+} ions ($[Ar]3d^4$). The calculated results are consistent with those of experimental observations that at a lower range of Mn concentrations ($x < 0.33$ in $CsMn_xTe_{2-x}O_6$), the oxidation state of Mn is 3+.

It is interesting to note that Te 5*s* states contribute to both the valence band maximum and the conduction band minimum region. According to the analyses on Te and Mn oxidation states as previously discussed, the compound $CsMn_{0.25}Te_{1.75}O_6$ should contain 6.25% of Te^{4+} and 81.25%

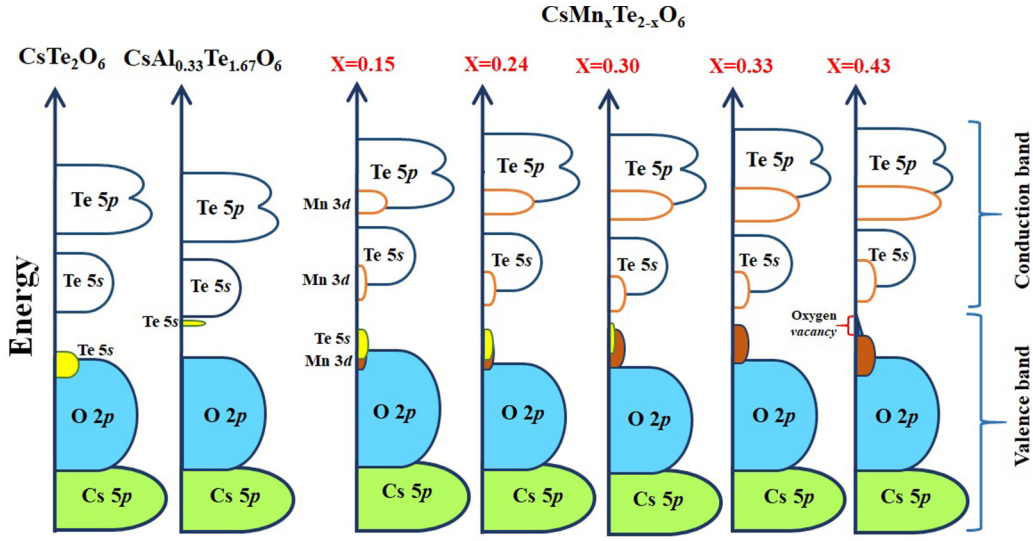

Mn Content	Top of VB; E_v (eV)	Bottom of conduction band; E_C (eV)	E_c–E_v (eV)	Activation energy; E_a (eV)
$CsTe_2O_6$	−1.24	0.12	1.36	1.15
$CsAl_{0.33}Te_{1.67}O_6$	−1.38	0.03	1.41	0.11
0.15	−0.28	0.42	0.70	0.63
0.24	−0.20	0.29	0.49	0.45
0.30	−0.08	0.16	0.24	0.24
0.33	−0.12	0.19	0.31	0.28
0.37	0	0.29	0.29	0.33
0.43	0	0.31	0.31	0.39

FIG. 9. The proposed schematic band structures of $CsMn_xTe_{2-x}O_6$.

of Te^{6+}. From a chemistry point of view, Te 5*s* states in the VB and the conduction band region originate from Te^{4+} and Te^{6+} in the samples, respectively. A similar feature is observed in $CsTe_2O_6$ [52]. In addition, the calculated DOS of $BaBiO_3$ also indicates the presence of Bi^{3+} 6*s* and Bi^{5+} 6*s* states in the VB and the conduction band, respectively [53]. Such a splitting of Te 5*s* band is a result of a local distortion which gives rise to a slightly longer Te^{4+}-O bond and more stabilized Te^{4+} 5*s* states. Without such a local distortion, the Te 5*s* band would be half-filled. In that case, the compound would become a type III mixed valency and exhibit metallic conducting behavior. Although not clearly observed in the XRD patterns, the split Te 5*s* states here suggest the presence of some local distortion resulting in a distinguishable Te^{4+}/Te^{6+}, and a type II mixed valency.

It can be seen from the discussion that the interpretation of frontier orbitals (VBM and conduction band maximum) are based mainly on the relative energies of Mn 3*d* and Te 5*s* states. Since the selection of the U value for Mn 3*d* electrons could affect the energy level of Mn 3*d* states, we carried out a DFT-generalized gradient approximation (GGA) calculation to gain more information about their relative energies. It can be seen from Ref. [54] that, in the absence of the U correction, the Mn 3*d* band does not split and most of Mn 3*d* states contribute solely in the A* and B* region, which contradicts the O *K*-edge spectra. Such a band diagram is expected because DFT suffers from the well-known self-interaction error and tends to over-delocalize electrons, which results in a wide Mn 3*d* band. Nevertheless, their overall features of frontier orbitals are quite similar where hybridization of Mn 3*d* and Te 5*s* states is predominant at the Fermi energy region of –1 to 1 eV.

To account for the electronic properties of the samples, we propose simple schematic band structures of the compounds as illustrated in Fig. 9, based on the XPS at the VB region, O *K*-edge XANES, and DFT calculated results. Previously reported band diagrams of $CsTe_2O_6$ and $CsAl_{0.33}Te_{1.67}O_6$ [52] are also shown for comparison. As concluded in Ref. [52], $CsTe_2O_6$ is an intrinsic semiconductor, while $CsAl_{0.33}Te_{1.67}O_6$ is an *n*-type semiconductor. When the energy differences between the top of the VB and the bottom of the conduction band ($E_c - E_v$) are compared with the activation energy of conduction obtained from the Arrhenius equation, all samples in $CsMn_xTe_{2-x}O_6$ series are intrinsic semiconductors. Therefore, the main factor that differentiates electronic behavior of $CsMn_xTe_{2-x}O_6$ from $CsAl_{0.33}Te_{1.67}O_6$ is the energy level of Te 5*s* orbital in the

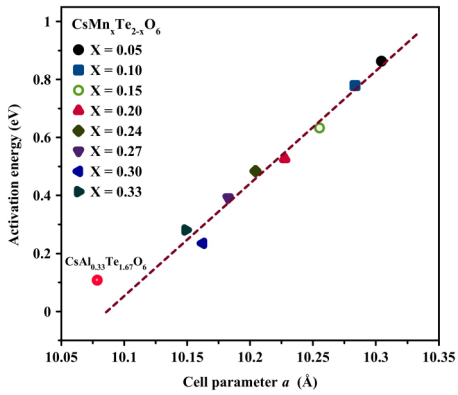

FIG. 10. Plots of cell parameters versus activation energy of $CsAl_{0.33}Te_{1.67}O_6$ and $CsMn_xTe_{2-x}O_6$ ($x = 0.05-0.33$).

VB, which is contributed by Te^{4+} in the compounds. Te^{4+} in $CsAl_{0.33}Te_{1.67}O_6$ is so compressed that its 5*s* state is considered a donor state whose energy level is very close to the conduction band minimum. On the other hand, because of the larger cell parameters in $CsMn_xTe_{2-x}O_6$ ($x < 0.33$), Te 5*s* states have low energy so that they overlap with Mn 3*d*-O 2*p* and become part of the VB. The correlation between cell parameters and activation energy of conduction is quite significant as a simple plot shown in Fig. 10 is roughly linear. Note that this correlation is obvious because both parameters are from the same series of compounds with similar electronic structure. When compared with other $Cs(M, Te)_2O_6$, other factors such as the energy level and diffusivity of *M* orbitals could result in some deviations.

This situation of $CsMn_xTe_{2-x}O_6$ is similar to that in $CsTe_2O_6$ although the hybridized Te 5*s*/*O* 2*p* in $CsMn_xTe_{2-x}O_6$ have slightly higher energy because of the smaller cell dimension. Yet, it seems that Te^{4+} is still not compressed enough to raise its energy level closer to the conduction band. It should be noted that there are much more Te^{4+} in $CsMn_xTe_{2-x}O_6$ ($x < 0.33$) than in $CsAl_{0.33}Te_{1.67}O_6$. Interestingly, if there are more Te^{4+} in $CsAl_{0.33}Te_{1.67}O_6$, they could form a defect band which might overlap with the conduction band giving rise to metallic-like conductors. On the other hand, if the energy of the Te 5*s* band in $CsMn_xTe_{2-x}O_6$ is raised, a similar outcome may be achieved. However, the number of Te^{4+} is correlated with the unit cell dimension and more Te^{4+} will expand the unit cell, hence lowering its energy level. Our attempts to increase the Te^{4+} content in other similar series with a smaller unit cell, namely $CsGe_{0.5}Te_{1.5}O_6$, was not successful because we cannot prepare single-phase compounds of $CsGe_xTe_{2-x}O_6$ with varied x.

As previously discussed, the samples with $x > 0.33$ contain a small amount of oxygen vacancies. XPS spectra at the VB region reveal an additional tailing as also included in the diagram (Fig. 9). Yet, the presence of such vacancies does not reduce $E_c - E_v$ difference nor the activation energy of conduction because their energy levels are quite low so that they too overlap with the VB. Similar observations are reported in Ref. [15], where oxygen deficient pyrochlores showed no improvement in the electronic conductivities.

V. CONCLUSION

Transformations of crystal structure and electronic property are observed in Mn substituted $CsTe_2O_6$. While the parent compound, $CsTe_2O_6$, is rhombohedral, substituting Mn into the lattice destroys the ordering resulting in a cubic structure. Simultaneously, the electronic conductivity increases by three orders of magnitude. To probe such transformations, a series of $CsMn_xTe_{2-x}O_6$ with $x = 0.05-0.43$ have been successfully prepared by solid state reaction. XPS and XANES were employed to determine the oxidation states and the substitution situation in the compounds. Based on our quantitative analyses of the data, the substitution can be represented by two different formulas. When x is lower than 0.33, Mn^{3+} replaces Te^{4+} resulting in $Cs^{1+}(Mn^{3+})_x(Te^{4+})_{0.5-(3x/2)}(Te^{6+})_{1.5+(x/2)}O_6$ cubic pyrochlores. The formation of this series of compounds is significant as it is clear and rare evidence that a significant amount of Te^{4+} could be stabilized in octahedral coordination. On the other hand, Te^{6+} are replaced by Mn^{3+} and Mn^{4+} when x is higher as can be described by $Cs^{1+}(Mn^{3+/4+})_x(Te^{6+})_{2-x}O_{6-\delta}$. The switching between the two schemes results in a sudden change in the cell parameter trend and the electrical properties. Based on the results from XPS at the VB region, O *K*-edge XANES, and computational calculation, both Mn 3*d* and Te 5*s* states significantly contribute to the frontier bands. The fact that there are two separated bands from Te 5*s* clearly indicates that the compound is a type II mixed valency with a distinguishable Te^{4+} and Te^{6+}. Though not observed in XRD, some local distortion must occur to stabilize Te^{4+} 5s states causing them to have lower energy and become part of a VB. As a result, the compounds are considered intrinsic semiconductors with small band gap energies.

ACKNOWLEDGMENTS

This work is financially supported by The National Research Council of Thailand, Suranaree University of Technology (SUT1-102-58-12-14) and the Research Network NANOTEC (RNN) program of the National Nanotechnology Center (NANOTEC), NSTDA, Thailand. We thank the synchrotron light research institute (public organization), Thailand, for PES, XPS, and XANES facilities.

[1] Z. Chen, W. Li, R. Li, Y. Zhang, G. Xu, and H. Cheng, Langmuir **29**, 13836 (2013).

[2] A. Alsac, A. Yildiz, T. Serin, and N. Serin, J. Appl. Phys. **113**, 063701 (2013).

[3] S. Cai, Y. Li, X. Chen, Y. Ma, X. Liu, and Y. He, J. Mater. Sci. Mater. Electron. **27**, 6166 (2016).

[4] M. B. Robin and P. Day, Adv. Inorg. Chem. Radiochem. **10**, 247 (1967).

[5] B. Baumert, J. Supercond. **8**, 175 (1995).

[6] S. Salem-Sugui, Jr, E. E. Alp, S. M. Mini, M. Ramanathan, J. C. Campuzano, G. Jennings, M. Faiz, S. Pei, B. Dabrowski, Y. Zheng, D. R. Richards, and D. G. Hinks, Phys. Rev. B **43**, 5511 (1991).

[7] B. Loopstra and K. Goubitz, Acta Crystallogr. Sec. C **42**, 520 (1986).

[8] A.W. Sleight, Physica C **514**, 152 (2015).

[9] T. Siritanon, G. Laurita, R. T. Macaluso, J. N. Millican, A. W. Sleight, and M. Subramanian, Chem. Mater. **21**, 5572 (2009).

[10] J. Li, T. Siritanon, J. K. Stalick, A. W. Sleight, and M. Subramanian, Inorg. Chem. **50**, 5747 (2011).

[11] T. Siritanon, A. Sleight, and M. Subramanian, Mater. Res. Bull. **46**, 2494 (2011).

[12] K. H. Zhang, Y. Du, A. Papadogianni, O. Bierwagen, S. Sallis, L. F. Piper, M. E. Bowden, V. Shutthanandan, P. V. Sushko, and S. A. Chambers, Adv. Mater. **27**, 5191 (2015).

[13] T. Hishida, K. Ohbayashi, M. Kobata, E. Ikenaga, T. Sugiyama, K. Kobayashi, M. Okawa, and T. Saitoh, J. Appl. Phys. **113**, 233702 (2013).

[14] K. Zhang, Y. Du, P. Sushko, M. E. Bowden, V. Shutthanandan, L. Qiao, G. Cao, Z. Gai, S. Sallis, and L. Piper, J. Phys.: Condens. Matter **27**, 245605 (2015).

[15] T. Siritanon, J. Li, J. K. Stalick, R. T. Macaluso, A. W. Sleight, and M. Subramanian, Inorg. Chem. **50**, 8494 (2011).

[16] See Supplemental Material at http://link.aps.org/supplemental/10.1103/PhysRevB.100.045132 for structure of $CsMn_{0.25}Te_{1.75}O_6$ model system.

[17] G. Kresse and J. Hafner, Phys. Rev. B **47**, 558 (1993).

[18] G. Kresse and J. Furthmüller, Phys. Rev. B **54**, 11169 (1996).

[19] G. Kresse and J. Furthmüller, Comput. Mater. Sci. **6**, 15 (1996).

[20] L. Li, X. Feng, Y. Nie, S. Chen, F. Shi, K. Xiong, W. Ding, X. Qi, J. Hu, and Z. Wei, ACS Catal. **5**, 4825 (2015).

[21] D. A. Tompsett, D. S. Middlemiss, and M. S. Islam, Phys. Rev. B **86**, 205126 (2012).

[22] C. Sun, Y. Wang, J. Zou, and S. C. Smith, Phys. Chem. Chem. Phys. **13**, 11325 (2011).

[23] D. A. Tompsett, S. C. Parker, P. G. Bruce, and M. S. Islam, Chem. Mater. **25**, 536 (2013).

[24] J. P. Perdew, K. Burke, and M. Ernzerhof, Phys. Rev. Lett. **77**, 3865 (1996).

[25] P. E. Blöchl, Phys. Rev. B **50**, 17953 (1994).

[26] G. Kresse and D. Joubert, Phys. Rev. B **59**, 1758 (1999).

[27] M. Subramanian, G. Aravamudan, and G. S. Rao, Prog. Solid. State. Chem. **15**, 55 (1983).

[28] L. Garvie and A. Craven, Phys. Chem. Mineral. **21**, 191 (1994).

[29] K. Sultan, M. Ikram, S. Gautam, H.-K. Lee, K. H. Chae, and K. Asokan, RSC Adv. **5**, 69075 (2015).

[30] B. Arun, M. Suneesh, B. Sudakshina, V. Akshay, K. Chandrasekhar, and M. Vasundhara, J. Phys. Chem. Solids **123**, 327 (2018).

[31] P. Thakur, K. Chae, C. Whang, G. Chang, D. Shukla, S. Mollah, and R. Kumar, J. Korean Phys. Soc. **53**, 1449 (2008).

[32] K. Asokan, Y. Chen, C. Pao, H. Tsai, C. O. Lee, C. Lin, H. Hsueh, D. Ling, W. Pong, and J. Chiou, Appl. Phys. Lett. **95**, 131901 (2009).

[33] D. Shukla, S. Mollah, R. Kumar, P. Thakur, K. Chae, W. Choi, and A. Banerjee, J. Appl. Phys. **104**, 033707 (2008).

[34] See Supplemental Material at http://link.aps.org/supplemental/10.1103/PhysRevB.100.045132 for Mn $2p$ XPS spectra of $CsMn_xTe_{2-x}O_6$.

[35] S. Daengsakul, S. Saengplot, P. Kidkhunthod, A. Pimsawat, and S. Maensiri, J. Magn. Magn. Mater. **451**, 435 (2018).

[36] See Supplemental Material at http://link.aps.org/supplemental/10.1103/PhysRevB.100.045132 for Te $3d$ XPS spectra and summary of Te components based on Te $3d_{5/2}$ XPS spectra of $CsMn_xTe_{2-x}O_6$.

[37] R. T. Shannon and C. T. Prewitt, Acta Crystallogr. Sec. B **25**, 925 (1969).

[38] R. D. Shannon, Acta Crystallogr. Sec. A. **32**, 751 (1976).

[39] See Supplemental Material at http://link.aps.org/supplemental/10.1103/PhysRevB.100.045132 for TEM analysis at different areas of $CsMn_{0.43}Te_{1.57}O_6$ sample.

[40] D. Groult, J. Pannetier, and B. Raveau, J. Solid State Chem. **41**, 277 (1982).

[41] S. Rahimnejad, J. H. He, W. Chen, K. Wu, and G. Q. Xu, RSC Adv. **4**, 62423 (2014).

[42] X. Wang, X. Wang, Q. Di, H. Zhao, B. Liang, and J. Yang, Materials **10**, 1398 (2017).

[43] R. Dudric, A. Vladescu, V. Rednic, M. Neumann, I. Deac, and R. Tetean, J. Mol. Struct. **1073**, 66 (2014).

[44] S. Van den Berghe, J.-P. Laval, B. Gaudreau, H. Terryn, and M. Verwerft, J. Nucl. Mater. **277**, 28 (2000).

[45] F. Wahoud, J. Guillot, J. Audinot, P. Bertrand, A. Delcorte, and H. Migeon, Appl. Surf. Sci. **293**, 85 (2014).

[46] E. Podgornov, I. Prosvirin, and V. Bukhtiyarov, J. Mol. Catal. A Chem. **158**, 337 (2000).

[47] Y. Lv, W. Yao, R. Zong, and Y. Zhu, Sci. Rep. **6**, 19347 (2016).

[48] H. Liu, J. Zhou, L. Zhang, Z. Hu, C. Kuo, J. Li, Y. Wang, L. H. Tjeng, T.-W. Pi, and A. Tanaka, J. Phys. Chem. C **121**, 16079 (2017).

[49] P. Balasubramanian, H. S. Nair, H. Tsai, S. Bhattacharjee, M. Liu, R. Yadav, J. Chiou, H. Lin, T. Pi, and M. Tsai, J. Elec. Spec. Rel. Phenom. **189**, 51 (2013).

[50] E. Pellegrin, L. Tjeng, F. De Groot, R. Hesper, G. Sawatzky, Y. Moritomo, and Y. Tokura, J. Elec. Spec. Rel. Phen. **86**, 115 (1997).

[51] M. Abbate, D. Cruz, G. Zampieri, J. Briatico, M. Causa, M. Tovar, A. Caneiro, B. Alascio, and E. Morikawa, Solid State Commun. **103**, 9 (1997).

[52] A. Waehayee, T. Eknapakul, N. Chanlek, T. Kongnok, S. Rattanasuporn, H. Nakajima, W. Meevasana, and T. Siritanon, J. Alloys. Compd. **718**, 215 (2017).

[53] C. Franchini, A. Sanna, M. Marsman, and G. Kresse, Phys. Rev. B **81**, 085213 (2010).

[54] See Supplemental Material at http://link.aps.org/supplemental/10.1103/PhysRevB.100.045132 for projected density of states of the $CsMn_{0.25}Te_{1.75}O_6$ model system calculated using the DFT-GGA method.